

This figure "fig1a.jpeg" is available in "jpeg" format from:

<http://arxiv.org/ps/astro-ph/9806226v1>

This figure "fig1b.jpeg" is available in "jpeg" format from:

<http://arxiv.org/ps/astro-ph/9806226v1>

This figure "fig1c.jpeg" is available in "jpeg" format from:

<http://arxiv.org/ps/astro-ph/9806226v1>

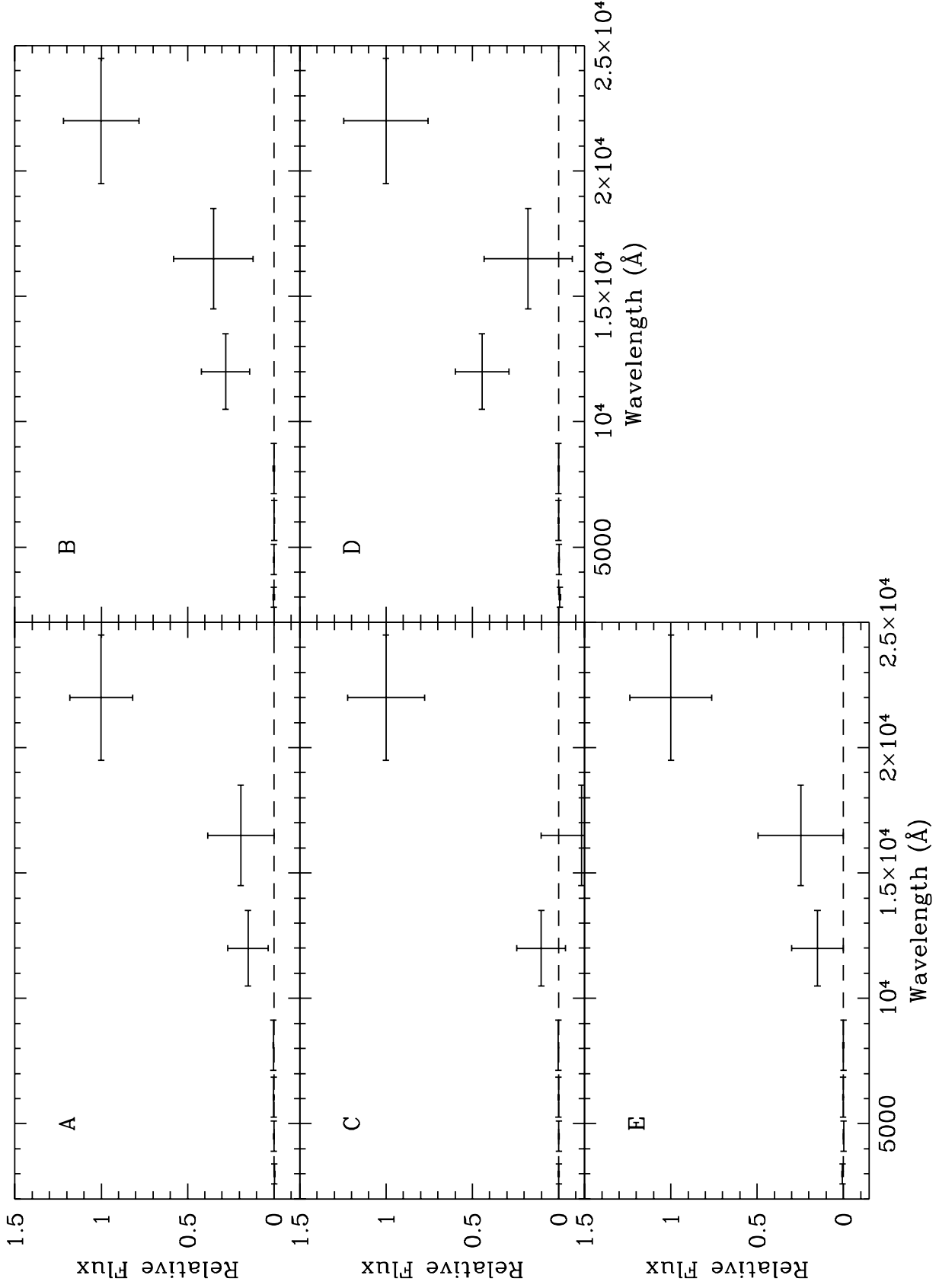
TABLE 2
 PROPERTIES OF EXTREMELY HIGH REDSHIFT GALAXY CANDIDATES

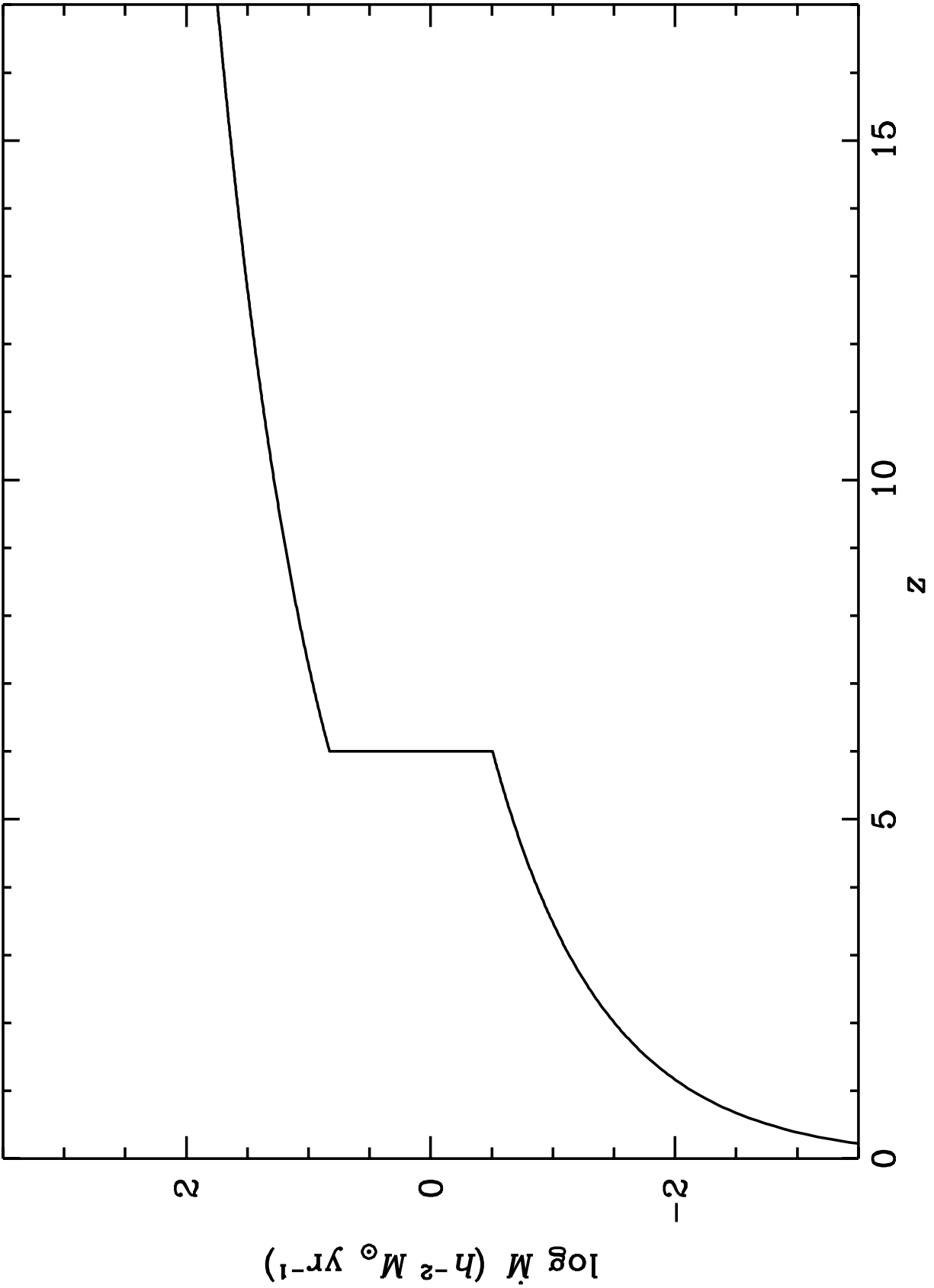
Galaxy	x	y	α	δ	$f_{\lambda}(3000)$	$f_{\lambda}(4500)$	$f_{\lambda}(6060)$	$f_{\lambda}(8140)$	$f_{\lambda}(12,000)$	$f_{\lambda}(16,000)$
A	115	481	12:36:56.3537	62:13:21.759	-0.003(0.003)	0.000(0.002)	0.001(0.001)	0.003(0.002)	0.150(0.117)	0.192(0.192)
B	528	454	12:36:47.9797	62:12:51.286	0.001(0.004)	0.000(0.002)	-0.002(0.002)	0.000(0.003)	0.280(0.140)	0.350(0.230)
C	647	112	12:36:48.6375	62:11:53.770	-0.001(0.003)	0.000(0.002)	0.000(0.001)	0.002(0.002)	0.101(0.141)	-0.131(0.232)
D	924	373	12:36:40.4616	62:12:14.004	-0.007(0.004)	-0.002(0.002)	0.000(0.001)	0.000(0.002)	0.444(0.156)	0.178(0.256)
E	281	453	12:36:53.1447	62:13:07.014	0.006(0.004)	-0.001(0.002)	0.002(0.001)	0.000(0.002)	0.151(0.151)	0.247(0.247)

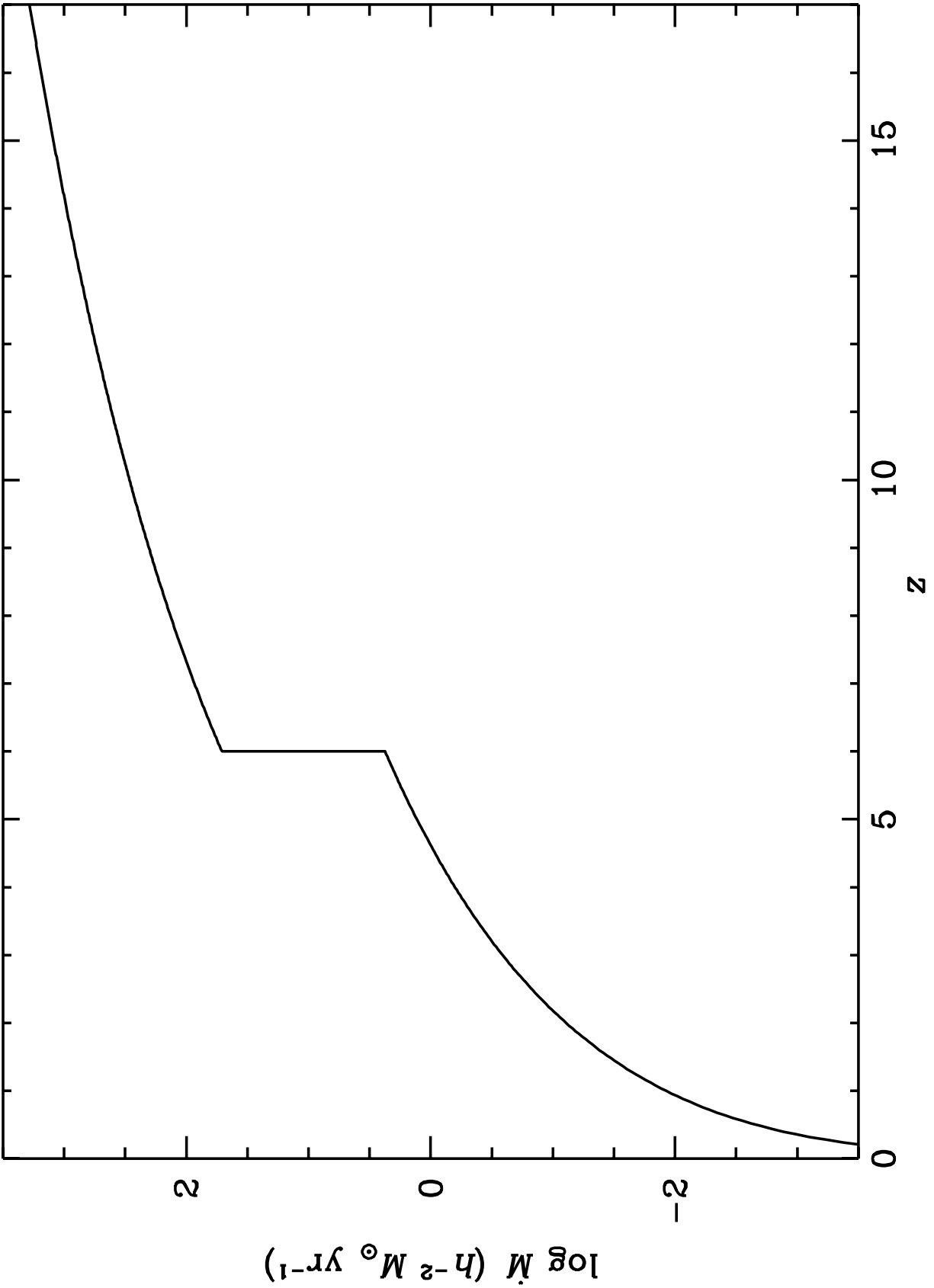
NOTE—Table lists galaxy, pixel values in the infrared image x and y , J2000 coordinates α and δ , fluxes $f_{\lambda}(3000)$, $f_{\lambda}(4500)$, $f_{\lambda}(6060)$, $f_{\lambda}(8140)$, $f_{\lambda}(12,000)$, $f_{\lambda}(16,000)$ to flux in K band, with flux uncertainties in parentheses, and magnitude $AB(22,000)$.

This figure "fig2.jpeg" is available in "jpeg" format from:

<http://arxiv.org/ps/astro-ph/9806226v1>







AN EMPIRICAL LIMIT ON EXTREMELY HIGH REDSHIFT GALAXIES^{1,2}

KENNETH M. LANZETTA and AMOS YAHIL

Department of Physics and Astronomy, State University of New York at Stony Brook
Stony Brook, NY 11794-3800, U.S.A.

and

ALBERTO FERNÁNDEZ-SOTO

School of Physics, University of New South Wales
P.O. Box 1, Kensington, NSW 2033, AUSTRALIA

arXiv:astro-ph/9806226v1 16 Jun 1998

¹Based on observations with the NASA/ESA Hubble Space Telescope, obtained at the Space Telescope Science Institute, which is operated by the Association of Universities for Research in Astronomy, Inc., under NASA contract NAS5-26555.

²Based on observations made at the Kitt Peak National Observatory, National Optical Astronomy Observatories, which is operated by the Association of Universities for Research in Astronomy, Inc. (AURA) under cooperative agreement with the National Science Foundation.

ABSTRACT

We apply the Lyman absorption signature to search for galaxies at redshifts $z \approx 6 - 17$ using optical and infrared images of the Hubble Deep Field. The infrared images are sensitive to a point source 5σ detection threshold of $AB(22,000) = 23.8$, which adopting plausible assumptions to relate rest-frame ultraviolet flux densities to unobscured star formation rates is easily sufficient to detect the star formation rates expected for massive elliptical galaxy formation to quite high redshifts. For $q_0 = 0.5$, the infrared images are sensitive to an unobscured star formation rate of $\dot{M} = 100 h^{-2} M_\odot \text{ yr}^{-1}$ to redshifts as large as $z = 17$, and for $q_0 = 0$, the infrared images are sensitive to an unobscured star formation rate of $\dot{M} = 300 h^{-2} M_\odot \text{ yr}^{-1}$ to redshifts as large as $z = 14$. The primary result of the analysis is that only one extremely high redshift galaxy candidate is identified at the 5σ level of significance (and four at the 4σ level). This implies a strict upper limit to the surface density of extremely high redshift galaxies of $< 1.5 \text{ arcmin}^{-2}$ to a limiting magnitude threshold $AB(22,000) = 23.8$. This also implies a strict upper limit to the volume density of extremely high redshift galaxies if (and only if) such galaxies are not highly obscured by dust.

Subject headings: galaxies: evolution

1. INTRODUCTION

A standard paradigm is that massive elliptical galaxies form most or all of their stars in a single rapid burst at early epochs. According to this scenario, early elliptical galaxies undergo a phase of intense ultraviolet luminosity, as the star formation rates required to produce $\approx 10^{11}$ stars in under $\approx 10^9$ yr exceed $100 M_{\odot} \text{ yr}^{-1}$. Recent progress in identifying galaxies at high redshifts has opened up the possibility of directly observing this epoch of massive elliptical galaxy formation. In particular, various analyses of the Hubble Deep Field (HDF) images obtained by the Hubble Space Telescope (HST) have identified galaxies with spectroscopically determined redshifts as large as $z \approx 4$ (Steidel et al. 1996; Lowenthal et al. 1997) and photometrically estimated redshifts as large as $z \approx 6$ (Lanzetta, Yahil, & Fernández-Soto 1996; Lanzetta, Fernández-Soto, & Yahil 1997). A primary result of these analyses is that the unobscured star formation rates of high-redshift galaxies inferred directly from the observed ultraviolet continua are surprisingly modest—typically less than $\approx 10 M_{\odot} \text{ yr}^{-1}$ and always well less than the $\approx 100 M_{\odot} \text{ yr}^{-1}$ or more expected for massive elliptical galaxy formation. Various proposals have been put forward to explain the apparent discrepancy between the expected and observed star formation rates, including the possibilities that (1) massive elliptical galaxies form at lower redshifts, say $z < 2.5$ (Madau et al. 1996), (2) massive elliptical galaxies form at redshifts $z \approx 3$ but are obscured by dust (Meurer et al. 1997), and (3) massive elliptical galaxies form at higher redshifts, say $z > 6$ (Maoz 1997).

The possibility that massive elliptical galaxies form at redshifts $z > 6$ is accessible to direct investigation by means of existing observations of the HDF. By combining images obtained at optical wavelengths by HST (Williams et al. 1996) with images obtained at infrared wavelengths by the Kitt Peak National Observatory (KPNO) 4 m telescope (Dickinson et al. 1998, in preparation), galaxies may in principle be detected at redshifts as large as $z \approx 17$, beyond which Ly α is redshifted past the response of the *K*-band filter. Such galaxies almost certainly must exhibit the same Lyman absorption signature characteristic of other high-redshift galaxies—namely complete absorption of flux below the Lyman limit and strong absorption of flux in the Ly α forest. The reason is that this signature is imprinted by intrinsic and intervening neutral hydrogen, which is observed to be abundant in the early universe. The Lyman absorption signature thus provides a robust and sensitive means of identifying extremely high redshift galaxy candidates or of establishing an empirical limit on extremely high redshift galaxies using broad-band photometric techniques.

Here we apply the Lyman absorption signature to search for galaxies at redshifts $z \approx 6 - 17$ using optical and infrared images of the HDF. Adopting plausible assumptions to relate rest-frame ultraviolet flux densities to unobscured star formation rates and adopting standard Friedmann cosmological models with dimensionless Hubble constant $h = H_0/(100 \text{ km s}^{-1} \text{ Mpc}^{-1})$, deceleration parameter in the range $q_0 = 0 - 0.5$, and zero cosmological constant, the infrared images are easily sensitive to the star formation rates expected for massive elliptical galaxy formation to quite high redshifts. For $q_0 = 0.5$, the infrared images are sensitive to an unobscured star formation rate of $\dot{M} = 100 h^{-2} M_{\odot} \text{ yr}^{-1}$ to redshifts as large as $z = 17$, and for $q_0 = 0$, the infrared images are sensitive to an unobscured star formation rate of $\dot{M} = 300 h^{-2} M_{\odot} \text{ yr}^{-1}$ to redshifts as large as

$z = 14$. The primary result of the analysis is that only one extremely high redshift galaxy candidate is identified at the 5σ level of significance (and four at the 4σ level), which implies a strict upper limit to the surface density of extremely high redshift galaxies and a strict upper limit to the volume density of extremely high redshift galaxies if (and only if) such galaxies are not highly obscured by dust.

2. METHOD

There are two reasons to believe that extremely high redshift galaxies must exhibit the same Lyman absorption signature that is characteristic of other high-redshift galaxies—namely complete absorption of flux below the Lyman limit and strong absorption of flux in the $\text{Ly}\alpha$ forest. First, extremely high redshift galaxies are probably optically thick to Lyman continuum absorption by intrinsic neutral hydrogen. This is because extremely high redshift galaxies are probably characterized by much higher gas fractions than nearby galaxies, which are observed to be optically thick to Lyman continuum absorption by intrinsic neutral hydrogen (Leitherer et al. 1995). Second, the extremely high redshift universe is probably optically thick to Lyman continuum and $\text{Ly}\alpha$ -forest absorption by intervening neutral hydrogen. This is because at the highest redshifts accessible to QSO absorption line measurements ($z \approx 3 - 5$), the universe is observed to be optically thick to Lyman continuum and $\text{Ly}\alpha$ -forest absorption, and the incidence of Lyman continuum and $\text{Ly}\alpha$ -forest absorption systems is observed to be increasing rapidly with increasing redshift. For example, the $\text{Ly}\alpha$ -forest flux decrement parameter D_A is observed to increase monotonically with redshift to a value $D_A = 0.7$ at $z \approx 5$ (Madau 1995), and a straightforward linear extrapolation of measurements of D_A over the redshift interval $z \approx 2.5 - 5$ predicts $D_A = 1$ (i.e. complete absorption of flux in the $\text{Ly}\alpha$ forest) by $z \approx 6.2$. At even higher redshifts—at epochs before galaxy formation depletes the intergalactic medium and before ionizing photons produced by massive stars ionize the intergalactic medium—the universe is almost certainly optically thick to smoothly distributed Lyman continuum and $\text{Ly}\alpha$ -forest Gunn–Peterson absorption.

For these reasons, we conclude that the Lyman absorption signature provides a robust and sensitive means of identifying extremely high redshift galaxy candidates or of establishing an empirical limit on extremely high redshift galaxies using broad-band photometric techniques. The method is to apply the Lyman absorption signature to identify extremely high redshift galaxy candidates using optical and infrared photometry in just the same way that the Lyman absorption signature is applied to identify other high-redshift galaxy candidates using optical photometry alone, namely by seeking objects that exhibit a precipitous spectral discontinuity across $\text{Ly}\alpha$. At redshifts $z > 6$ the Lyman absorption signature is redshifted beyond observed-frame optical wavelengths, hence extremely high redshift galaxy candidates must be identified as objects that are (1) detected at infrared wavelengths and (2) not detected to within sensitive upper limits at optical wavelengths.

The major uncertainty in using photometric techniques to estimate redshifts of extremely high redshift galaxies is that owing to the lack of background probes the optical depth to $\text{Ly}\alpha$ -forest

absorption has not yet been measured at redshifts beyond $z \approx 5$. Here we assume that at redshifts $z > 6$ the optical depth to Ly α -forest absorption approaches $\tau \rightarrow \infty$, which is consistent with the trend established at lower redshifts. In this case, at infrared wavelengths galaxies may in principle be detected at redshifts as large as $z \approx 17$, beyond which Ly α is redshifted past the response of the K -band filter.

3. ANALYSIS

The optical images were obtained by HST in December, 1995 using the Wide Field Planetary Camera 2 (WFPC2) and the F300W, F450W, F606W, and F814W filters (Williams et al. 1996). The infrared images were obtained by the KPNO 4 m telescope in April, 1996 using the IRIM camera and standard J , H , and K filters (Dickinson et al. 1998, in preparation). Our previous analysis (Lanzetta, Yahil, & Fernández-Soto 1996) identified objects in the F814W image, the faintest of which is of total magnitude $AB(8140) \approx 30$. The goal of the current analysis is to identify objects in regions of the infrared images not occupied by objects detected at optical wavelengths.

First, we measured the point spread functions of the infrared images by fitting Gaussian profiles to stars detected in the images. We accounted for variations of the point spread functions across the images by fitting the variations of the FWHM of the point spread functions versus positions from the centers of the images by quadratic polynomials. Next, we masked objects detected at optical wavelengths from the infrared images by setting the values of pixels associated with objects identified in the F814W image equal to zero. We located such pixels by modeling the spatial profile of every object detected in the F814W image as a convolution of the portion of the F814W image containing the object with the appropriate point spread function of the K -band image and fitting the model spatial profiles to the K -band image to define isophotal mask regions. Next, we measured the noise characteristics of the infrared images by determining the empirical covariances of the masked images. The infrared images are significantly correlated over adjacent pixels, hence off-diagonal terms of the empirical covariances must be included in order to determine accurate photometric uncertainties. Finally, we searched for objects detected in the infrared images by forming the “point source flux images” and corresponding “point source flux variance images” from the masked images. [We expect high-redshift galaxies to appear as point sources in the infrared images because our previous analysis (Lanzetta, Yahil, & Fernández-Soto et al. 1996) indicates that high-redshift galaxies are no more than several tenths arcsec across, which is much less than the FWHM ≈ 1 arcsec point spread functions of the infrared images.] The optimally-weighted point source flux at pixel i, j is

$$F(i, j) = \frac{\sum_{i', j'} f(i', j') \Phi(i - i', j - j')}{\sum_{i', j'} \Phi^2(i', j')}, \quad (1)$$

and the optimally-weighted point source flux variance at pixel i, j is

$$\text{var}[F(i, j)] = A \frac{\sum_{i', j'} \sigma^2(i', j') \Phi^2(i - i', j - j')}{[\sum_{i', j'} \Phi^2(i', j')]^2}, \quad (2)$$

where $f(i, j)$ is the flux at pixel i, j , $\sigma^2(i, j)$ is the flux variance at pixel i, j , $\Phi(i, j)$ is the point spread function at pixel i, j , and A is a factor of order unity that accounts for off-diagonal terms of the empirical covariance and where the sums extend over all pixels covered by the point spread function. The point source flux images are shown in Figure 1, and the point source 5σ detection thresholds determined from the point source flux variance images are listed in Table 1. Objects detected in the infrared images are identified by comparing pixels of the point source flux images with corresponding pixels of the point source variance images. The limiting magnitude thresholds are $AB(12,000) = 24.3$, $AB(16,000) = 23.7$, and $AB(22,000) = 23.8$.

The result of the search is that one object at the 5σ level of significance and four objects at the 4σ level of significance are detected in the K -band image. We designate these objects as objects A through E in order of decreasing flux. No objects are detected in the J - or H -band images at the 5σ level of significance. Properties of the objects are listed in Table 2, K -band and F814W images of the objects are shown in Figure 2, and the spectral energy distributions of the objects are shown in Figure 3. The solid angle Ω of the portion of the infrared images included into the analysis is $\Omega = 5.1 \text{ arcmin}^2$, and the fraction f of the portion of the infrared images included into the analysis and associated with objects identified in the F814W image is $f = 0.33$. The solid angle $\Omega(1 - f)$ of the portion of the infrared images included into the analysis and not associated with objects identified in the F814W image is $\Omega(1 - f) = 3.4 \text{ arcmin}^2$.

We performed several tests of the reality of objects A through E as follows: First, we sought to identify negative fluctuations in the images employing exactly the same techniques used to identify positive fluctuations in the images. No negative fluctuations were detected in the J -, H -, or K -band images at the 4σ or greater level of significance. Next, we estimated probabilities of detecting chance 4 or 5σ fluctuations, assuming a Gaussian distribution of noise fluctuations. The portion of the infrared images included into the analysis is made up of ≈ 4000 independent resolution elements, over which the probability of detecting a chance 5σ fluctuation is just 1.2×10^{-8} and of a chance 4σ fluctuation is just 1.2×10^{-4} . Finally, we sought to verify the objects in independent K -band images obtained by Hogg et al. (1996) with the Keck telescope. The Keck images (which cover only a small portion of the HDF) include only object D, which occurs at the very edge of the Keck image 2. Object D is present in the Keck image, with a flux consistent with the value measured from the KPNO image. We conclude that objects A through E are likely to be real rather than chance fluctuations.

4. IMPLICATIONS

The primary result of the analysis is that only one extremely high redshift galaxy candidate is identified at the 5σ level of significance (and four at the 4σ level), which implies strict upper limits to the surface and volume densities of extremely high redshift galaxies. Here we consider the 5σ level of significance threshold in order to establish conservative limits that are unlikely to be contaminated by spurious detections.

Following Steidel et al. (1996) and Lowenthal et al. (1997), we use the spectral synthesis models of Leitherer, Robert, & Heckman (1995) to relate rest-frame ultraviolet flux densities to unobscured star formation rates. We adopt a power-law relationship between monochromatic luminosity density L_λ and wavelength λ

$$L_\lambda(\lambda) \propto \lambda^{-\beta} \quad (3)$$

and express unobscured star formation rate \dot{M} in terms of monochromatic luminosity density $L_{\lambda_{1500}}$ at rest-frame wavelength $\lambda = 1500 \text{ \AA}$ as

$$\dot{M} = \frac{L_{\lambda_{1500}}}{1.4 \times 10^{40} \text{ erg s}^{-1} \text{ \AA}^{-1}} M_\odot \text{ yr}^{-1}. \quad (4)$$

Equation (4) applies for a continuous star formation model with a Salpeter (1955) initial mass function of upper mass cutoff $M_{\text{up}} = 80M_\odot$. A continuous star formation model is appropriate because the star formation time scale is expected to be no less than the dynamical time scale, which for massive elliptical galaxies is much longer than massive star lifetimes. We adopt $\beta = 1.2$, which is consistent with measurements of nearby starburst galaxies and galaxies with spectroscopically determined redshifts $z \approx 3$ in the HDF (Meurer et al. 1997) and with our own measurements of galaxies with photometrically estimated redshifts $z \approx 5$ in the HDF. For the adopted value of β , the J - and K -band images reach almost identical levels of sensitivity to star formation while the H -band image reaches a lower level of sensitivity to star formation. For this reason, we consider only the K -band image to identify extremely high redshift galaxies at all redshifts $z \approx 6 - 17$.

The unobscured star formation rate corresponding to the 5σ detection threshold of the K -band image at redshifts $z = 6 - 17$ is shown in Figure 3. [For comparison, the unobscured star formation rate corresponding to the 5σ detection threshold of the F814W image at redshifts $z = 0 - 6$ is also shown in Figure 3. This rate is calculated assuming a limiting magnitude threshold of $AB(8140) = 28.0$.] For $q_0 = 0.5$, the infrared images are sensitive to an unobscured star formation rate of $\dot{M} = 30 h^{-2} M_\odot \text{ yr}^{-1}$ to redshifts as large as $z = 12$ and of $\dot{M} = 100 h^{-2} M_\odot \text{ yr}^{-1}$ to redshifts as large as $z = 17$. For $q_0 = 0$, the infrared images are sensitive to an unobscured star formation rate of $\dot{M} = 100 h^{-2} M_\odot \text{ yr}^{-1}$ to redshifts as large as $z = 7$ and of $\dot{M} = 300 h^{-2} M_\odot \text{ yr}^{-1}$ to redshifts as large as $z = 14$.

The result that only one extremely high redshift galaxy candidate is identified at the 5σ level of significance establishes a 3σ upper limit of 5.2 to the mean number of extremely high redshift galaxies over the area and volume sampled by the masked images. The solid angle sampled by the masked images is 3.4 arcmin^{-2} , and the corresponding 3σ upper limit to the surface density Σ of extremely high redshift galaxies to a limiting magnitude threshold $AB(22,000) = 23.8$ is $\Sigma < 1.5 \text{ arcmin}^{-2}$. The comoving volume sampled by the masked images between redshifts $z_{\text{min}} = 6$ and $z_{\text{max}} = 7 - 17$ is listed in Table 3. For $q_0 = 0.5$, the corresponding 3σ upper limit to the comoving volume density n of extremely high redshift galaxies with unobscured star formation rates exceeding $\dot{M} = 30 h^{-2} M_\odot \text{ yr}^{-2}$ is $n < 1.8 \times 10^{-3} h^3 \text{ Mpc}^3$ and exceeding $\dot{M} = 100 h^{-2} M_\odot \text{ yr}^{-2}$ is $n < 1.2 \times 10^{-3} h^3 \text{ Mpc}^3$. For $q_0 = 0$, the corresponding 3σ upper limit to the comoving

volume density n of extremely high redshift galaxies with unobscured star formation rates exceeding $\dot{M} = 100 h^{-2} M_{\odot} \text{ yr}^{-2}$ is $n < 3.7 \times 10^{-4} h^3 \text{ Mpc}^3$ and exceeding $\dot{M} = 300 h^{-2} M_{\odot} \text{ yr}^{-2}$ is $n < 3.1 \times 10^{-5} h^3 \text{ Mpc}^3$.

5. DISCUSSION

The 3σ upper limits to the comoving volume density of extremely high redshift galaxies derived from analysis of the HDF images are substantially lower (by factors of between 3 and 180) than the volume density $n = 5.6 \times 10^{-3} h^3 \text{ Mpc}^{-3}$ of nearby luminous ($L > L_*$) galaxies (Ellis et al. 1996). This implies that either (1) early elliptical galaxies are obscured by dust, (2) intense star formation in early elliptical galaxies occurs with a short duty cycle, or (3) massive elliptical galaxies do not form at redshifts $z > 6$. Although these possibilities cannot be distinguished on the basis of the current observations, certain arguments can be brought to bear on their merits.

First, it is presumably the case that the very first star formation in early elliptical galaxies is not obscured by dust, simply because the first dust is produced by the first generation of stars. Adopting the plausible assumption that star formation and the subsequent mixing of dust with gas cannot take place across an entire galaxy on a time scale that is much less than the dynamical time scale, then the dust-free phase of early galaxies could last for a significant fraction of the relevant dynamical time scale, which for massive elliptical galaxies is $\approx 10^8 \text{ yr}$. Unless massive elliptical galaxy formation occurred at exceptionally high redshifts (i.e. $z > 30$), this phase of galaxy formation should persist through $z < 17$ and hence be in reach of direct observation, especially for cosmological models with large values of the deceleration parameter. Second, it is unlikely that intense star formation in early elliptical galaxies occurs on time scales much less than the dynamical time scale. Again, unless massive elliptical galaxy formation occurred at exceptionally high redshifts, this phase of galaxy formation should be in reach of direct observation. Although not conclusive, the evidence seems to indicate that massive elliptical galaxies did not form at redshifts $z > 6$.

If, in spite of the arguments put forward above, galaxies at the very early epochs probed by the infrared images of the HDF are obscured by even moderate amounts of dust, then of course substantially higher star formation rates are allowed. For example, recent evidence suggests that galaxies of redshift $z \approx 3$ suffer extinction of $E(B - V) \approx 0.1$, which corresponds to an ultraviolet attenuation of a factor of several, depending on details of the extinction curve (e.g. Pettini et al. 1997). If such a factor applies to the galaxies probed by the infrared images of the HDF, then star formation rates as large as $\approx 1000 M_{\odot} \text{ yr}^{-1}$ cannot be ruled out by the present observations.

The upper limits to the comoving volume density of extremely high redshift galaxies derived from analysis of the HDF images are far more stringent—both in terms of sensitivity to star formation and of comoving volume sampled—than the upper limits derived from other searches for high-redshift galaxies at infrared wavelengths based on emission lines such as [O II] $\lambda 3727$ and H β

(e.g. Thompson, Djorgovski, & Beckwith 1994). The reason is that the analysis of the HDF images is based on broad-band photometric techniques, which probe far greater depths than narrow-band techniques. The infrared images obtained by the KPNO 4 m telescope are not the deepest images that can be obtained with existing telescopes. We expect that the Lyman absorption signature applied to even deeper infrared images obtained with ground- or space-based telescopes will either identify a significant population of extremely high redshift galaxies or will establish a much more interesting empirical limit on extremely high redshift galaxies.

Objects A through E are plausible candidates of galaxies at extremely high redshifts. Or they might be very cool stars of surface temperature $T < 1400$ K, although there is some indication that at least some of the objects are spatially resolved. These objects are prime targets for future observations.

We are grateful to M. Dickinson for providing access to the reduced infrared images and to an anonymous referee for providing helpful comments. This research was supported by NASA grant NAGW-4422 and NSF grant AST-9624216.

TABLE 1
POINT SOURCE 5σ DETECTION THRESHOLDS

Image	AB	Detection Threshold	
		f_ν ($\text{erg s}^{-1} \text{cm}^{-2} \text{Hz}^{-1}$)	f_λ ($\text{erg s}^{-1} \text{cm}^{-2} \text{\AA}^{-1}$)
J	24.3	6.8×10^{-30}	1.4×10^{-19}
H	23.7	1.2×10^{-29}	1.4×10^{-19}
K	23.8	1.1×10^{-29}	6.8×10^{-20}

TABLE 3
COMOVING VOLUME

z_{\max}	V (Mpc ³)	
	$q_0 = 0$	$q_0 = 0.5$
7	14,020	609
8	30,037	1150
9	48,039	1633
10	68,017	2069
11	89,964	2464
12	113,877	2825
13	139,749	3157
14	167,579	3462
15	197,363	3745
16	229,101	4008
17	262,789	4253

REFERENCES

- Ellis, R. S., Colless, M., Broadhurst, T., Heyl, J., & Glazebrook, K. 1996, *MNRAS*, 280, 235
- Hogg, D. W., Neugebauer, G., Armus, L., Matthews, K., Pahre, M. A., Soifer, B. T., & Weinberger, A. J. 1996, *AJ*, 113, 474
- Lanzetta, K. M., Fernández-Soto, A., & Yahil, A. 1997, *ApJ*, submitted
- Lanzetta, K. M., Yahil, A., & Fernández-Soto, A. 1996, *Nature*, 381, 759
- Leitherer, C., Ferguson, H. C., Heckman, T. M., & Lowenthal, J. D. 1995, *ApJ*, 454, L19
- Leitherer, C. & Heckman, T. M. 1995, *ApJS*, 96, 9
- Leitherer, C., Robert, C., & Heckman, T. M. 1995, *ApJS*, 99, 173
- Lowenthal, J. D., Koo, D. C., Guzmán, R., Gallego, J., Phillips, A. C., Faber, S. M., Vogt, N. P., Illingworth, G. D., & Gronwall, C. 1997, *ApJ*, 481, 673
- Madau, P. 1995, *ApJ*, 441, 18
- Madau, P., Ferguson, H. C., Dickinson, M. E., Giavalisco, M., Steidel, C. C., & Fruchter, A. 1996, *MNRAS*, 283, 1388
- Maoz, D. 1997, *ApJ*, submitted
- Meurer, G. R., Heckman, T. M., Lehnert, M. D., Leitherer, C., & Lowenthal, J. 1997, *AJ*, in press
- Pettini et al. 1997, in *Origins*, ASP Conference Series, ed. J. M. Shull, C. E. Woodward, & H. Thronson (San Francisco: Astronomical Society of the Pacific), in press
- Salpeter, E. E. 1955, *ApJ*, 121, 1610
- Steidel, C. C., Giavalisco, M., Pettini, M., Dickinson, M., & Adelberger, K. L. 1996, *ApJ*, 462, L17
- Thompson, D., Djorgovski, S., & Beckwith, S. V. W. 1994, *AJ*, 107, 1
- Williams, R. E., et al. 1996, *AJ*, 112, 1335

Fig. 1.— Point source flux images determined from the (a) J -, (b) H -, and (c) K -band infrared images obtained by the KPNO 4 m telescope. Angular extent of each image is 163×163 arcsec². Black represents high flux and white represents low flux. Solid gray areas indicate regions of the infrared images occupied by objects detected at optical wavelengths in the optical images obtained by HST. The angular extent of the infrared images is slightly larger than the angular extent of the optical images, hence no objects are detected at optical wavelengths along the edges of the infrared images or above and to the right of the location of the Planetary Camera (i.e. in the upper right corner).

Fig. 2.— K -band and F814W images of objects A through E. Angular extent of each image is 30×30 arcsec². Black represents high flux and white represents low flux. Tic marks indicate objects. K -band images have been processed for optimal detection of point sources, as described by equation (1).

Fig. 3.— Spectral energy distributions of objects A through E. Vertical error bars show flux uncertainties, and horizontal error bars show filter FWHM.

Fig. 4.— Logarithm of unobscured star formation rate \dot{M} vs. redshift z for (a) $q_0 = 0.5$ and (b) $q_0 = 0$. Star formation rate is calculated according to equations (3) and (4) assuming a limiting magnitude threshold of $AB(22,000) = 23.8$ at redshifts $z = 6 - 17$ and a limiting magnitude threshold of $AB(8140) = 28.0$ at redshifts $z = 0 - 6$.